Journal of Nuclear Materials 407 (2010) 34–43

Contents lists available at ScienceDirect

Journal of Nuclear Materials

journal homepage: www.elsevier.com/locate/jnucmat

The role of irradiated microstructure in the localized deformation of austenitic stainless steels

Z. Jiao *, G.S. Was

University of Michigan, Department of Nuclear Engineering and Radiological Sciences, Ann Arbor, MI 48109, United States

ABSTRACT

Localized deformation has emerged as a potential factor in irradiation-assisted stress corrosion cracking of austenitic stainless steels in LWR environments and the irradiated microstructure may be a critical factor in controlling the degree of localized deformation. Seven austenitic alloys with various compositions were irradiated using 2–3 MeV protons to doses of 1 and 5 dpa at 360 °C. The irradiated microstructure consisting of dislocation loops and voids was characterized using transmission electron microscopy. The degree of localized deformation was characterized using atomic force microscopy on the deformed samples after conducting constant extension rate tension tests to 1% and 3% strain in argon. Localized deformation was found to be dependent on the irradiated microstructure and to correlate with hardening originating from dislocation loops. Dislocation loops enhance the formation of dislocation channels and localize deformation into existing channels. On the contrast, voids mitigate the degree of localized deformation. The degree of localized deformation decreases with SFE with the exception of alloy B. Localized deformation was found to have similar dependence on SFE as loop density suggesting that SFE affects localized deformation by altering irradiated microstructure.

1. Introduction

Irradiation-assisted stress corrosion cracking (IASCC) has been a critical problem of core component cracking in light water reactors (LWRs) since its discovery. It is a very complex phenomenon and can be affected by a number of factors such as radiation-induced segregation (RIS), radiation hardening and irradiated microstructure. Although these factors have been recognized for decades, their roles in IASCC are still under debate. For instance, both RIS and irradiation hardening may contribute to IASCC to some extent but neither is the primary cause as suggested by the post-irradiation annealing experiments [1]. Other processes may be a factor and localized deformation has been identified as one such process that may have a major impact on IASCC [2]. Experiments by Hash et al. [2] showed that localized deformation was much more prominent in proton-irradiated 304 SS samples that cracked than in those that did not, drawing attention to the possible role of localized deformation in IASCC. Onchi et al. [3,4] found that crack initiation sites tended to be related to the deformation bands in sensitized 304 SS. Recent work has shown the possible contribution of localized deformation to IASCC [5–8] in proton-irradiated austenitic alloys under simulated BWR environment.

Dislocation channeling is an important deformation mode in alloys under light water reactor operating conditions. Deformation of irradiated austenitic alloys is highly localized in coarse dislocation channels. The average dislocation channel height on a free surface can be as great as a few hundred nanometers in irradiated austenitic alloys, which corresponds to hundreds or thousands of dislocations [6]. When this number of dislocations interacts with the grain boundary at a single location, the local area of the grain boundary will sustain substantial stress and/or strain. Cracks were observed to initiate at the intersection of dislocation channels and grain boundaries in austenitic alloys under simulated BWR environment [8], which indicated an apparent link between localized deformation and IASCC. A correlation between localized deformation and IASCC is being established and will be published elsewhere.

Although dislocation channels have been experimentally shown to correlate with surface slip steps [9,10], the mechanism of the formation of dislocation channels is still not well understood. The formation of dislocation channels involves the interaction between a group of dislocations [11,12] and the irradiation-induced defects such as defect clusters, dislocation loops, voids, precipitates etc. This process can be very intricate. Studies on the interactions between dislocations and irradiation-induced defects have been focused on simulations. Molecular dynamics simulations have shown that moving dislocations can shear, annihilate or partially annihilate defects resulting in defect debris and/or imperfections such as jogs on the dislocations [13,14]. It is therefore deduced that the nature and strength of the irradiation-induced defects may affect the formation and evolution of dislocation channels.

---

* Corresponding author.
E-mail address: zjiao@umich.edu (Z. Jiao).

0022-3115/$ - see front matter © 2010 Elsevier B.V. All rights reserved.
doi:10.1016/j.jnucmat.2010.07.006

It has been hypothesized that the degree of localized deformation may vary with stacking fault energies (SFEs) [5]. This is because that dislocation slip behavior is affected by SFE. Dislocations in low SFE alloys tend to glide in a planar fashion while in high SFE alloys wavy slip is common due to dislocation cross-slip. In irradiated alloys, the interactions between dislocations and irradiation-induced defects are expected to be affected by SFEs, which also contribute to localized deformation. In austenitic alloys, stacking fault energies are known to be dependent on compositions. By varying alloy compositions, differences in irradiation microstructures and the degree of localized deformation may be achieved. The objective of this paper is to explore how the irradiation microstructure contributes to localized deformation in proton-irradiated austenitic alloys with various SFEs.

2. Experimental

Seven austenitic alloys with various Ni and Cr content were selected for this study. The compositions of these alloys are shown in Table 1. The SFEs, predicted by Pickering's correlation [15] and characterized using transmission electron microscopy (TEM) by measuring the separation between partial dislocations [16], are also shown in Table 1. It would be ideal to select alloys that only vary in Ni and Cr content so that the effect of minor elements such as Si and P on IASCC can be minimized. However, the low Ni concentration in high purity low SFE alloys is usually not sufficient to retain the full austenite phase. Therefore, commercial grade alloy A was included because of its very low SFE.

Except for commercial grade alloy A, the other six alloys are high purity alloys made at the General Electric Company by arc-melting followed by a series of hot rolling process to a total reduction of ~50% in thickness. The alloys were then solution annealed to achieve relatively uniform microstructure. The average grain size ranged from 40 to 60 μm with the ASTM grain size number between 5.5 and 7. All the alloys were used in the as-received condition. TEM bars and tensile samples of these alloys were fabricated by Shular Tools Company. The dimensions of the tensile sample are shown in Fig. 1. The TEM bars with dimensions of 2 mm × 2 mm × 20 mm served as spacers in between tensile bars and were used to characterize the irradiated microstructure. They were irradiated at the same conditions as the tensile bars. Irradiation microstructures were characterized using these TEM bars.

Prior to proton irradiations, the TEM bars and tensile samples were ground using SiC grinding papers to a final grit of #4000. The samples were then electropolished for 30 s in a 10% perchloric acid in 90% methanol solution at −40 °C to remove surface residual damage due to mechanical grinding.

Irradiations were performed using 2–3 MeV protons in a Tandetron accelerator at the Michigan Ion Beam Laboratory (MIBL). Two batches of samples were irradiated to 1 and 5 dpa, respectively. During the irradiation, the temperature was kept within 360 ± 10 °C by balancing the amount of cooling and heating applied to the sample stage. The dose rate was calculated to be $\sim 8 \times 10^{-6}$ dpa/s using the TRIM code [17]. Penetration depth of protons at 2 MeV is 25 μm and at 3 MeV, the depth is 40 μm. A more detailed description of the proton irradiation procedure can be found elsewhere [18].

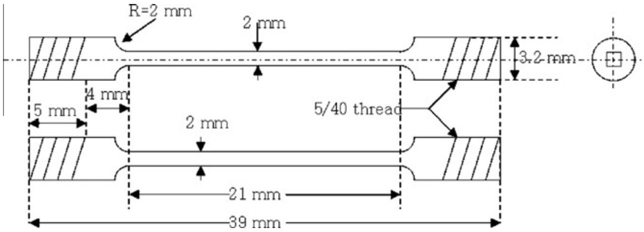

Fig. 1. Dimensions of a tensile bar.

After each irradiation, the TEM bars were ground from the unirradiated surface to ~200 μm and 3-mm TEM disks were then cut from the irradiated TEM bars using an ultrasonic slurry cutter. The disks were further mechanically thinned to ~100 μm from the unirradiated surface using a gravity feed lapping device from Gatan, Inc. The disks were then electropolished from the irradiated surface for ~7 s in a 5% perchloric acid and 95% methanol solution at −50 °C using a single jet thinner. The final TEM foils were obtained by jet-thinning from the backside (unirradiated) in the same solution until perforation occurred. This procedure produced the transparent areas of TEM foils at a depth of 5–10 μm from the irradiated surface.

Dislocation loops and voids were examined using a JOEL 2010F analytical electron microscope at the University of Michigan Electron Microbeam Analysis Laboratory (EMAL). Faulted dislocation loops were imaged using dark field rel-rod technique [19]. TEM foils were tilted to near [0 1 1] beam direction, the rel-rods due to the edge-on faulted dislocation loops can be seen in the diffraction pattern. Part of the edge-on dislocation loops then can be imaged by selecting one of the rel-rods. The edge-on dislocation loops are shown as short straight lines in the dark field images. Note that only dislocation loops on one of the four sets of (1 1 1) planes were imaged using rel-rod technique therefore the number was multiplied by four to get the correct number of loops. The foil thickness was determined from the electron energy-loss spectrum (EELS) by measuring the ratio of the zero loss peak intensity to that of the total spectrum [20]. The EELS was only obtained from the local area where the dislocation loops were imaged. Voids were examined using conventional bright field under slight underfocus condition.

Radiation-induced segregation (RIS) at grain boundaries were measured via STEM/EDS using the JEOL 2010F instrument at the Electron Microbeam Analysis Laboratory at the University of Michigan and the Philips CM200/FEG TEM-STEM at the Oak Ridge National Laboratory on the same samples used for microstructure analysis. The CM200/FEG operates with an accelerating voltage of 200 kV and an incident beam size <1.4 nm (full-width at one tenth

Table 1
Compositions (wt.%) and stacking fault energies of selected alloys.

Alloy	Nominal	Fe	Cr	Ni	Mn	Si	P	C	SFE (mJ/m^2)	
									Predicted[a]	Measured
A	18Cr8Ni	Bal.	18.30	8.50	1.38	0.65	0.03	0.04	25.2	15.5
B	18Cr12Ni	Bal.	17.49	11.87	0.98	0.11	0.014	0.02	39.3	19.7
C	15Cr12Ni	Bal.	15.76	12.04	0.98	0.10	<0.01	0.02	41.3	28.0
D	22Cr15Ni	Bal.	22.00	15.00	1.00	0.10	NM	0.02	42.9	38.2
E	13Cr15Ni	Bal.	13.41	15.04	1.03	0.10	<0.01	0.016	47.7	36.3
F	18Cr25Ni	Bal.	18.00	25.00	1.00	0.03	0.01	0.02	66.0	47.1
G	21Cr32Ni	Bal.	20.73	31.16	0.94	0.10	0.014	0.014	72.7	61.1

[a] Predicted from Pickering's correlation [15]. NM = not measured.

maximum (FWTM) of the electron beam intensity). The 2010F operates at 200 kV with an incident beam size of ~1.1 nm FWTM. The grain boundary was aligned to edge-on position prior to each measurement. The bulk compositions were used to calculate the *k*-factors so that the grain boundary chemistry can be determined.

Constant extension rate tensile (CERT) tests were performed on the irradiated tensile bars in an argon atmosphere at 288 °C with a strain rate of $3.5 \times 10^{-7}\ \mathrm{s}^{-1}$. In order to examine localized deformation at different stain levels, all the tests were interrupted at 1% and 3% plastic strain.

The degree of localization due to dislocation channeling can be characterized by several unique quantities such as spacing between channels, channel width and channel height. However, dislocation channel height which is proportional to the number of dislocations in the channel is believed to be the most important quantity in relating channeling to IASCC. Each glide dislocation in the channel generates a displacement equivalent to its Burgers vector, **b**. Dislocation channels intersecting the sample surface appear as slip steps on the surface, which can be clearly observed in optical or scanning electron microscope (SEM). The height of the slip steps (dislocation channels), are measured using atomic force microscope (AFM).

Due to the limitation of the AFM sample stage, the entire tensile sample cannot be accommodated. Therefore, the channel height was characterized using high resolution replicas. The replicas constitute a smaller specimen, which is better suited for AFM analysis and a durable archive of the specimen surface at each strain increment. The replicas were made using the Microset replica kits. The reproduction of the sample surface is a key factor in using replicas for surface analysis. Previous work [21] showed that the replica can accurately reproduce the surface and the features of the slip channels can be faithfully preserved. An average of 60 dislocation channels was characterized for each condition.

Since channels with largest steps are more likely to initiate cracks when they intersect grain boundaries, the weighted average channel height was used to represent a channel height distribution as shown in the following equation:

$$\bar{h} = \frac{\sum_{i=1}^{n} h_i^2}{\sum_{i=1}^{n} h_i}, \tag{1}$$

where h_i is the channel height of *i*th dislocation channel. The weighted average channel height puts more weight on the larger channels. As the distribution of channel height is skewed to the larger channels, the weighted average channel height is generally larger than the mathematical average.

3. Results and discussion

3.1. Irradiated microstructure

Dislocation loops were observed in all the alloys at both 1 and 5 dpa. Voids were found in only a few alloys under certain conditions. Dislocation loop and void sizes and densities are summarized in Table 2. Fig. 2 shows some selected TEM dark field images of dislocation loops and bright field images of voids in alloys A–C and G irradiated to 1 and 5 dpa at 360 °C. As shown in Fig. 2, the size and density of both dislocation loops and voids vary with alloy and irradiation dose. A full comparison of the mean dislocation loop diameter, dislocation loop density, mean void size,

Table 2

Summary of the characterization results of the microstructure, hardness, change in yield stress and localized deformation following irradiation of alloys A–G to 1 and 5 dpa at 360 °C. NM means "not measured".

Dose	Alloy	Microstructure				Hardness			Calculated change in yield strength				Weighted average channel height (nm)/spacing (μm)	
		Mean loop diameter (nm)	Loop density ($10^{22}\ \mathrm{m}^{-3}$)	Void size (nm)	Void density ($10^{22}\ \mathrm{m}^{-3}$)	Unirradiated (kg/mm^2)	Irradiated (kg/mm^2)	Hardening (kg/mm^2)	$\Delta\sigma_{\mathrm{loops}}$ (MPa)	$\Delta\sigma_{\mathrm{voids}}$ (MPa)	$\Delta\sigma_{\mathrm{micros}}$ (MPa)	$\Delta\sigma H_v$ (MPa)	1% strain	3% strain
1 dpa	A	3.6 ± 0.1	3.20 ± 0.30	–	–	187.0 ± 5.8	266.8 ± 14.5	79.0 ± 15.6	315	0	315	239.4	197/8	311/NM
	B	7.1 ± 0.2	1.05 ± 0.08	3.4	0.11	150.0 ± 2.0	213.4 ± 12.5	63.4 ± 12.7	251	112	275	192.1	122/NM	239/4
	C	6.6 ± 0.3	2.22 ± 0.32	–	–	137.7 ± 5.6	231.9 ± 12.7	94.2 ± 13.9	352	0	352	285.4	255/NM	351/NM
	D	7.3 ± 0.4	0.81 ± 0.07	2.5	<0.1	135.2 ± 3.8	206.4 ± 14.8	71.2 ± 15.3	224	0	224	215.7	NM	NM
	E	6.9 ± 0.3	2.40 ± 0.30	3.0	<0.01	137.2 ± 6.3	238.8 ± 12.2	101.6 ± 13.7	374	0	374	307.8	190/7	288/NM
	F	8.7 ± 0.4	1.09 ± 0.08	–	–	153.1 ± 10.1	246.3 ± 9.4	93.2 ± 13.8	283	0	283	282.4	168/4.5	231/NM
	G	7.9 ± 0.5	1.89 ± 0.20	–	–	145.6 ± 6.5	243.7 ± 17.3	98.1 ± 18.5	357	0	357	297.2	119/NM	180/NM
5 dpa	A	5.7 ± 0.2	6.81 ± 0.80	–	–	184.1 ± 8.3	363.0 ± 21.9	178.8 ± 23.4	574	0	574	541.8	401/10	420/NM
	B	7.4 ± 0.2	3.03 ± 0.19	5.8	0.77	145.3 ± 6.4	314.5 ± 11.7	169.2 ± 13.3	437	387	584	512.7	139/NM	313/NM
	C	7.8 ± 0.3	2.72 ± 0.20	3.2	0.37	130.8 ± 6.2	301.3 ± 14.6	170.5 ± 15.9	421	201	467	516.6	322/NM	364/NM
	D	8.2 ± 0.2	3.95 ± 0.60	3.9	1.32	140.4 ± 7.6	321.3 ± 14.1	180.9 ± 16	523	417	669	548.1	313/NM	360/NM
	E	8.2 ± 0.2	2.88 ± 0.29	2.5	0.41	132.2 ± 6.7	327.9 ± 16.0	195.4 ± 17.3	458	185	494	592.1	322/7.8	393/NM
	F	10.9 ± 0.2	3.52 ± 0.53	4.8	0.03	134.0 ± 4.4	329.8 ± 10.3	195.8 ± 11.2	570	66	574	593.3	305/NM	348/NM
	G	9.8 ± 0.6	1.99 ± 0.30	4.2	0.93	134.1 ± 5.6	338.3 ± 22.8	204.2 ± 23.5	395	367	539	618.7	146/NM	314/NM

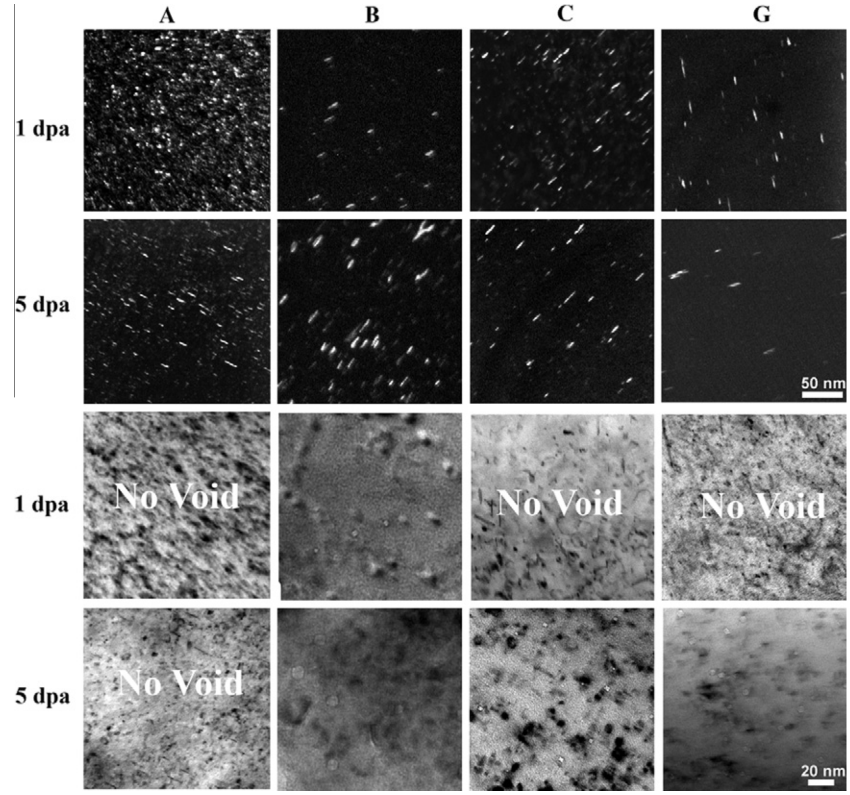

Fig. 2. TEM dark field images of dislocation loops and bright field images of voids in alloys A–C and G irradiated to 1 and 5 dpa at 360 °C.

void density and calculated swelling in all the seven alloys is shown in Fig. 3a–e. The mean loop diameters were similar in alloys B–E, at around 7 nm at 1 dpa and 8 nm at 5 dpa. Larger loops were found in alloys F and G (8.7 and 7.9 nm, respectively, at 1 dpa and 10.9 and 9.8 nm, respectively, at 5 dpa) and smaller loops were found in the commercial grade alloy A (3.6 nm at 1 dpa and 5.7 nm at 5 dpa). Loop number densities ranged from $0.8 \times 10^{22}\ \mathrm{m}^{-3}$ in alloy D to $2.4 \times 10^{22}\ \mathrm{m}^{-3}$ in alloy E at 1 dpa, and 2.0×10^{22} in alloy G to $3.9 \times 10^{22}\ \mathrm{m}^{-3}$ in alloy D at 5 dpa in high purity alloys. The loop density was significantly higher in the commercial grade alloy A for both doses. Both loop diameters and densities are in good agreement with previous studies [22].

A low density of voids was observed in alloys B–E at 1 dpa. Voids were observed in all alloys at 5 dpa except for alloy A where no voids were observed for both doses. The high density of dislocation loops and the absence of voids in commercial grade alloy A may be due to the higher content of Si (0.65 wt.%) compared to the other alloys (~0.1 wt.%). Silicon is known to enhance the diffusivity of vacancies and reduce the vacancy supersaturation [23,24] and is an effective swelling inhibitor [25].

The largest void size and highest density of voids were observed in alloy B at both doses. Swelling is the greatest in alloy B (0.079%) followed by alloys D (0.041%) and G (0.036%). High nickel content alloy F (18Cr25Ni) and lower chromium content alloy C (15Cr12Ni) has significantly less swelling (0.002% and 0.006%, respectively) than alloy B (18Cr12Ni) (0.079%). This is consistent with the literature that swelling decreases with increasing Ni content and decreasing Cr content [26,27].

The grain boundary Cr content at 1 and 5 dpa is shown in Fig. 4. The grain boundary Cr content is the highest in alloy D and the lowest in alloy C and E. The grain boundary Cr content shows some degree of dependence on the bulk Cr content since alloy D has the highest bulk Cr (22 wt.%) and alloy C and E have the lowest bulk Cr content (15 wt.% and 13 wt.%, respectively). The deviation of Cr content at grain boundaries from the bulk composition for each of the irradiated alloys is shown in Fig. 4. All alloys except for alloy A at 1 dpa exhibit depletion of Cr at grain boundaries. The higher-than-bulk Cr content at the grain boundary is due to the initial enrichment of Cr prior to irradiation. The grain boundary Cr concentration continued to decrease with dose and at 5 dpa the grain boundary Cr is lower than the bulk content by 2.3 wt.%. Alloys F and G have a larger degree of Cr depletion than other alloys. Alloy E, which has the lowest bulk Cr content, shows the least of depletion.

3.2. Irradiation hardening

The hardness and irradiation hardening are summarized in Table 2. Irradiation hardening was calculated as the difference in hardness before and after irradiation. Irradiation hardening in alloys A–G irradiated to 1 and 5 dpa is shown in Fig. 5. Irradiation hardening is approximately the same level for alloys C, E–G following irradiation to 1 dpa and corresponds to an increase of 90–100 $\mathrm{kg/mm^2}$ in hardness. The increase in hardness for alloys B and D is only 60–70 $\mathrm{kg/mm^2}$. Alloy A has a moderate increase in hardness (80 $\mathrm{kg/mm^2}$) but its hardness after irradiation is the greatest (267 $\mathrm{kg/mm^2}$). After 5 dpa, the hardness values for alloys B–G are comparable, while the commercial grade alloy A still has the greatest hardness.

An increase in yield strength due to irradiation is normally observed in irradiated alloys. This change can be readily measured by conducting tensile tests if the sample is fully irradiated. However, due to the limited penetration of 2–3 MeV protons, only small portion of the tensile samples (~20–40 μm) was irradiated, which has only a minor effect on the yield strength from tensile tests of these proton-irradiated samples. However, the change in yield strength can be estimated using the following empirical relation [28] in austenitic stainless steels:

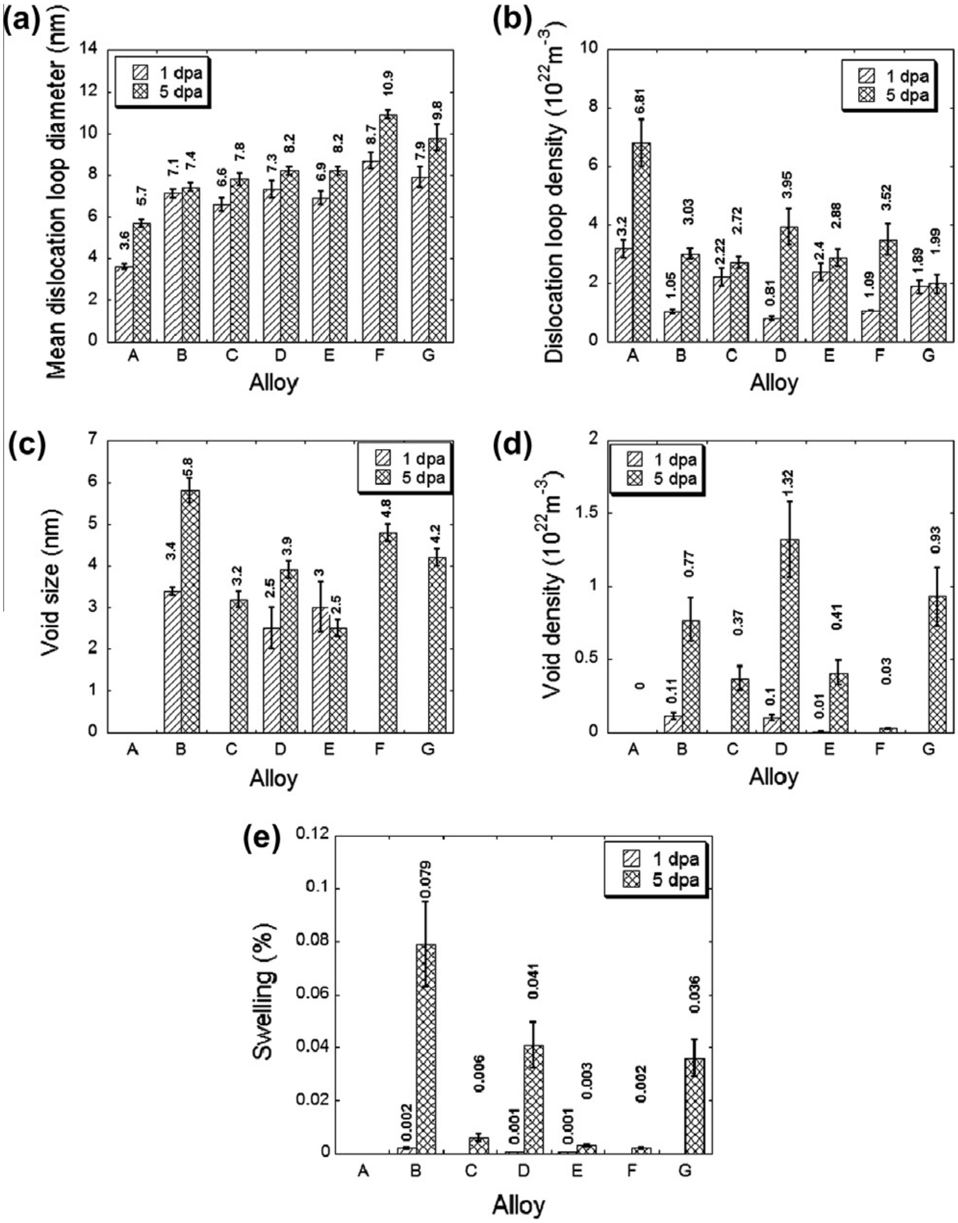

Fig. 3. Comparisons of (a) mean dislocation loop diameter, (b) loop density, (c) void size, (d) void density and (e) swelling among seven alloys irradiated to 1 and 5 dpa at 360 °C. The error bars are the standard error of the mean.

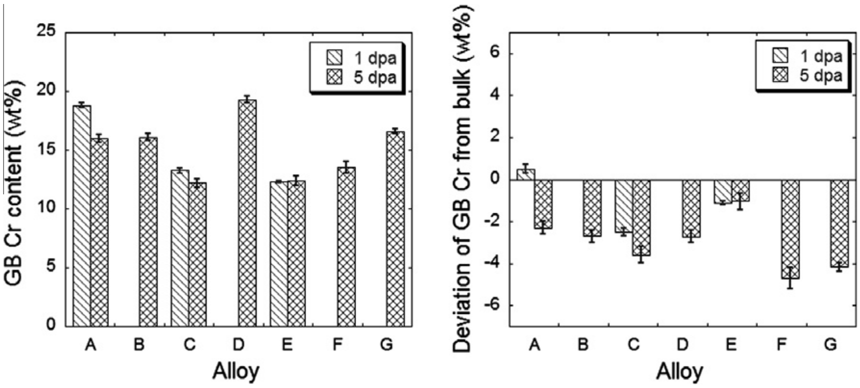

Fig. 4. Measured grain boundary Cr composition (left) and Cr deviation from bulk composition for alloys A–G irradiated to 1 and/or 5 dpa at 360 °C. The error bars are the standard error of the mean.

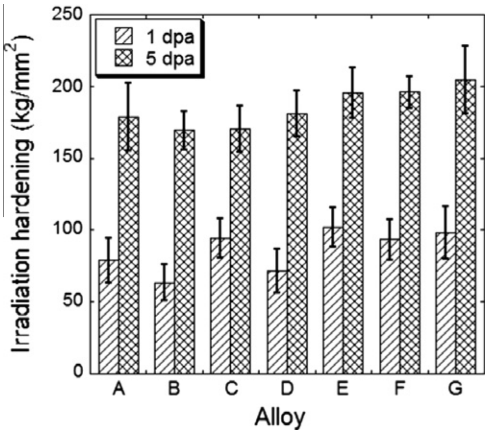

Fig. 5. Irradiation hardening in alloys A–G irradiated to 1 and 5 dpa at 360 °C. The error bars indicate the standard deviation.

$$\Delta\sigma_y = 3.03\Delta H_V \quad (2)$$

where ΔH_V is the increment of hardness in kg/mm^2 due to irradiation and $\Delta\sigma_y$ is the yield strength increment in MPa.

The change in yield strength in proton-irradiated alloys originates from the irradiated microstructure (dislocation loops, voids, etc.), therefore it can also be estimated using the dispersed-barrier hardening model [29] if the irradiated microstructure is quantitatively characterized. For instance, the change in yield strength due to dislocation loops and voids can be calculated using the following equations [30]:

$$\Delta\sigma_y = M\alpha\mu b(Nd)^{0.5} \quad (3)$$

$$\Delta\sigma_{\text{micros}} = (\Delta\sigma^2_{\text{loops}} + \Delta\sigma^2_{\text{voids}})^{0.5} \quad (4)$$

where N is the number density of obstacles, d is the mean diameter of the obstacle, μ is the shear modulus of the matrix, $\mathbf{b}$ is the Burgers vector of the moving dislocation, and M is the Taylor factor ($M = 3.06$, [31]). The barrier strength α for loops and voids was determined by a regression analysis of the data that resulted in values 0.5 for loops and 1.0 for voids. The total change in yield strength from irradiated microstructures ($\Delta\sigma_{\text{micros}}$) includes the contribution from both dislocation loops and voids as shown in Eq. (4).

The calculated changes in yield strength from dislocation loop and void microstructure as well as from measured irradiation hardening for each alloy are listed in Table 2 and are compared in Fig. 6. The 45° line in the figure represents a one-to-one correlation between yield strength change from measurement and from that calculated from the microstructure. In general, the two values are in good agreement, indicating that the measured loop and void size distributions account for the measured hardness changes.

3.3. Localized deformation

The calculated weighted average channel heights from AFM measurement for the seven alloys irradiated to 1 and 5 dpa and strained to 1% and 3% are listed in Table 2 and shown in Fig. 7a. In general, the weighted average channel height varies among the seven alloys and increases with strain and dose. The channel height is greatest in alloy A irradiated to 5 dpa and strained to 3% (420 nm) and smallest in alloy G irradiated to 1 dpa and strained to 1% (119 nm).

The distribution of slip channels also varies with alloy, irradiation dose and strain. Fig. 7b shows the height distribution of dislocation channels in alloy G irradiated to 1 dpa and strained to 1% as compared to alloy A irradiated to 5 dpa and strained to 3%. Both distributions are skewed to the right, which means for both cases there are a few exceptionally large channels. However, the largest channels in alloy A are more than twice the height of the largest channels in alloy G. Alloy A also has a broader distribution in height (50–850 nm).

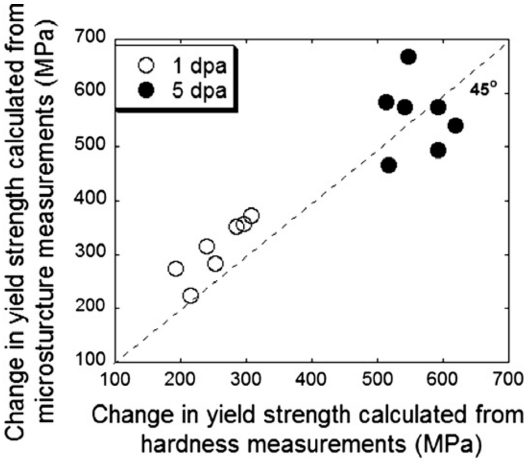

Fig. 6. A comparison of change in yield strength calculated from hardening and change in yield strength calculated from dislocation and void microstructure for alloys A–G irradiated with protons to 1 and 5 dpa at 360 °C. $\alpha = 0.5$ for loops and $\alpha = 1.0$ and for voids.

3.4. Correlation of irradiation microstructure with localized deformation

The irradiated microstructure can have a profound influence on the deformation mode [32]. Dislocation channeling was found to be the dominant deformation mode in all seven alloys irradiated to 1 and 5 dpa and tested in argon at 288 °C. The initiation of dislocation channels requires the coordinated movement of a group of dislocations in order to be able to annihilate the irradiation-induced defects [11]. As the formation of dislocation channels involves the interaction between the group of dislocations and dislocation loops and voids, the size and density of dislocation loops and voids may correlate with the degree of localized deformation in dislocation channels. In Fig. 8, the weighted average channel height was plotted as a function of dislocation loop size (8a), loop density (8b), void size (8c) and void density (8d) under the same irradiation conditions. There is no apparent correlation between channel height and dislocation loop size. However, the channel height increases with loop density. Weighted average channel height tends to be larger in the alloys with a high density of dislocation loops. Neither larger voids nor higher void density leads to larger degree of localized deformation as shown in 8c and 8d. On the contrary, channel height tends to decrease with void size and density.

As another way of examining the effect of irradiated microstructure on localized deformation, the weighted average channel height was plotted against the change in yield strength calculated from irradiated microstructure using Eq. (4) for 1% and 3% strain in Fig. 9a and b, respectively. The encircled points have contributions from both dislocation loops and voids. No clear correlation between channel height and change in yield strength can be observed from these two plots. Fig. 9c and 9d shows the same plots as 9a and 9b but the contribution from the voids for the encircled points are excluded, causing the points to "move" to the left along the x-axis. A correlation between channel height and the change in yield stress due to dislocation loops can be clearly observed. The weighted average channel height increases with the irradiation hardening due to dislocation loops even though the data are quite

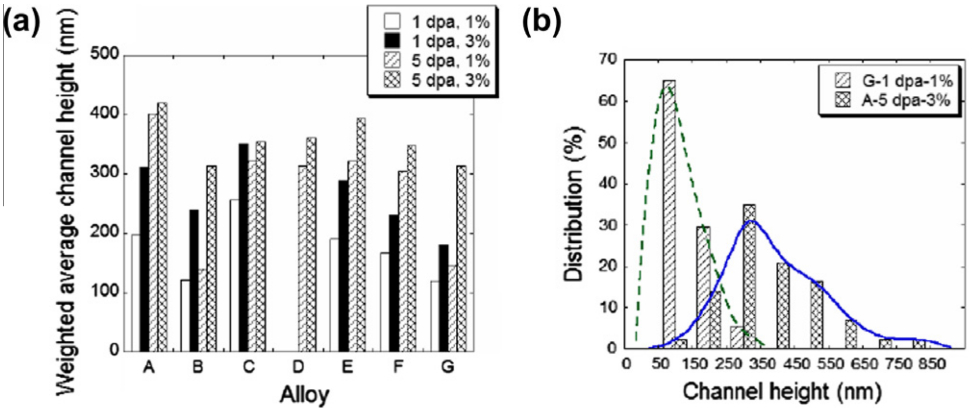

Fig. 7. (a) A comparison of weighted average channel height in alloys A–G irradiated to 1 and 5 dpa at 360 °C and strained to 1% and 3% in argon at 288 °C. (b) Distribution of channel height in alloy G irradiated to 1 dpa and strained to 1% and alloy A irradiated to 5 dpa and strained to 3% in argon.

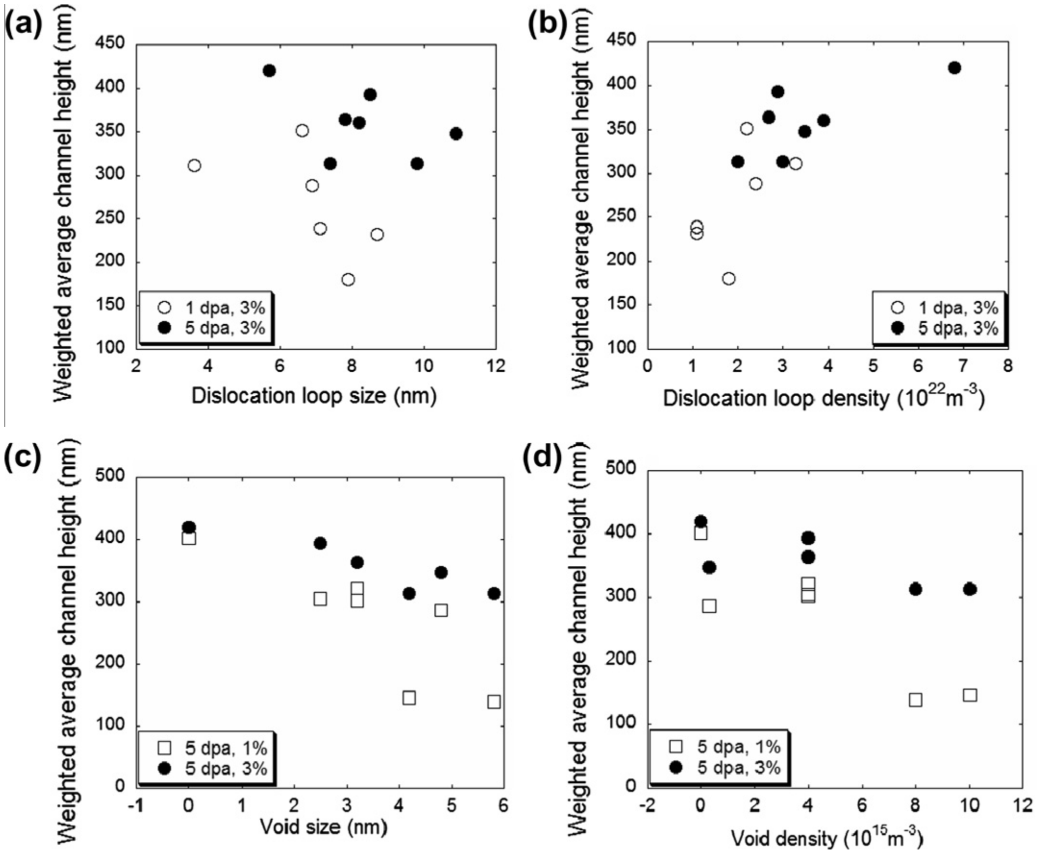

Fig. 8. Dependence of weighted average channel height on (a) dislocation loop size, (b) loop density, (c) void size and (d) density. Dislocation loops and voids were characterized in alloys A–G irradiated to 1 or 5 dpa at 360 °C. The channel heights were characterized on the seven alloys irradiated to 1 or 5 dpa at 360 °C and strained to 1% or 3% in argon at 288 °C. The irradiation dose and strain are shown in the legend for each plot.

scattered between the two parallel lines. This means that it is dislocation loops that promote localized deformation.

The dislocation sources for initiating dislocation channels can be irregular sites along grain boundaries, grown-in dislocations that are pinned by defect clusters or small loops or other stress risers in the matrix such as inclusions [33]. Regardless of the initiation sites, the dislocation sources are initially suppressed or locked by the irradiation-induced defects. A critical stress is required to activate the dislocation sources to initiate dislocation channels. A higher critical stress is expected in alloys with a higher degree of hardening originated from dislocation loops and voids. Once the critical stress is reached, dislocation channels are rapidly formed (on the order of milliseconds [34]) and usually with a substantial initial displacement [35]. Dislocation channels then continue to grow during the following straining till saturated [6]. Apparently, the initiation of dislocation channels and the initial displacement in the channel are affected by the irradiation-induced defects.

The channel height at a certain strain interval is the result of the total number of dislocations that have slipped in the dislocation channel. Therefore, the average channel height depends on weather deformation favors the initiation of new dislocation channels or

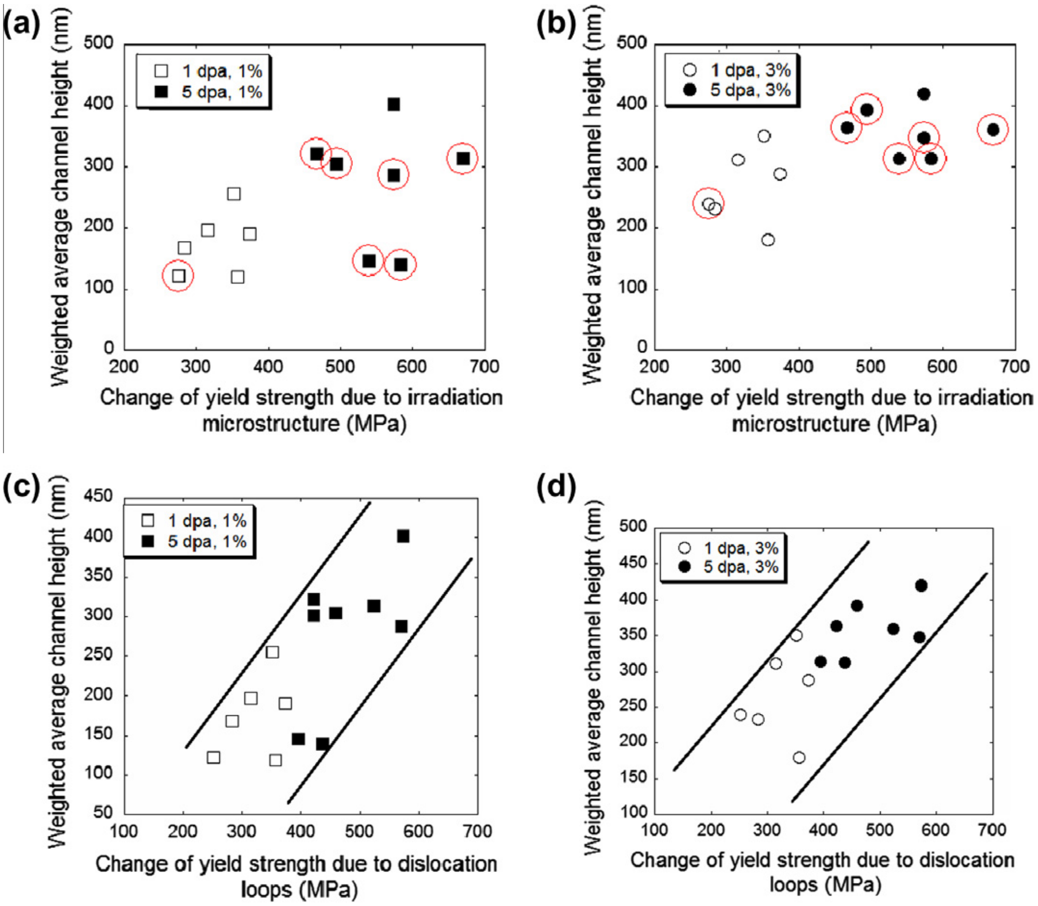

Fig. 9. Dependence of weighted average channel height on change in yield strength due to irradiated microstructure. The weighted average channel height was characterized at 1% (a) and (c) and 3% (b) and (d). The open symbols indicate that the alloys were irradiated to 1 dpa and the filled symbols are the alloys irradiated to 5 dpa at 360 °C. The large open circles in (a) and (b) indicate that the change in yield strength include the contribution from both dislocation loops and voids. The contribution of voids in (a) and (b) for the encircled points are excluded in (c) and (d).

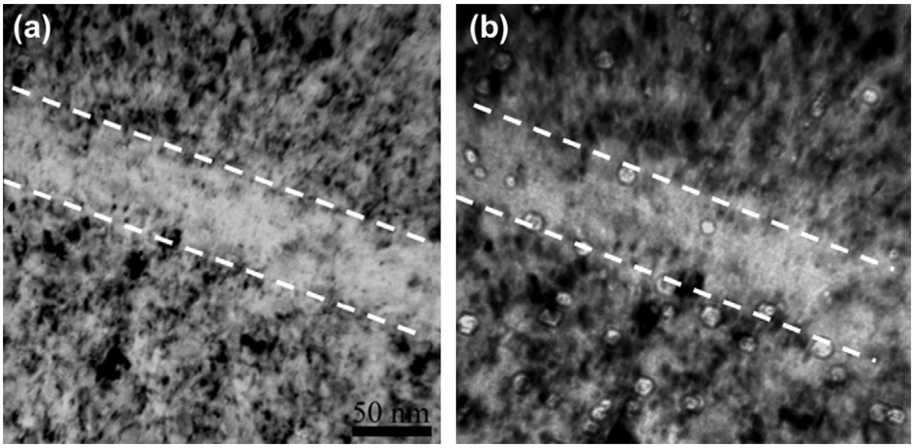

Fig. 10. TEM image of alloy B irradiated to 5 dpa at 360 °C and strained to 7% in argon at 288 °C showing (a) a dislocation channel relatively clear of dislocation loops (b) voids in the channel and (b) was taken at slight underfocus condition.

the continuous operation of existing channels during straining following yield. Obviously, the latter results in larger average channel height or a larger amount of slip or deformation in the channels. The relative hardening arising from obstacles in the channel and the surrounding matrix should determine how dislocation channels behave. The obstacles in the matrix include dislocation loops and voids. The so-called "defect-free" dislocation channels are, indeed, not free of defects. Fig. 10 shows TEM images of a dislocation channel in alloy B irradiated to 5 dpa at 360 °C and strained to 7% in argon at 288 °C. Fig. 10a shows the channel in focus. Although the defect density is significantly lower than that of the surrounding matrix, the channel is not completely free of defects. The contrast due to loop debris or remaining defect clusters is still visible in the channel. Fig. 10b was taken under slight underfocus condition. Note that voids are present in the channel, indicating that the dislocation loops can be completely or partially removed by glide dislocations but voids are not affected. Therefore, the obstacles in the channel include the residual dislocation loops and voids. Dislocations in the channel also need to overcome the back stress due to pile-up dislocations [7]. The population of voids in the channel is virtually unchanged from the matrix so they do not contribute to the channeling process. However, the density of dislocation loops is significantly less in the channel than in the matrix, meaning that hardening from dislocation loops changes significantly between the dislocation channels and matrix.

In the alloys with a higher density of dislocation loops, the hardening in the matrix due to dislocation loops is expected to be much larger than that in the channels. Thus, initiation of new dislocation channels is not favored. For instance, as shown in Table 2, alloy A irradiated to 5 dpa has the highest density of dislocation loops ($6.8 \times 10^{22}\ \mathrm{m}^{-3}$) while alloy F irradiated to 1 dpa has very low loop density ($1.1 \times 10^{22}\ \mathrm{m}^{-3}$). When these two alloys were strained to 1% in argon, the average spacing between channels in alloy A was 10 μm and the weighted average channel height was 401 nm. In alloy F, however, the average spacing between channels was only 4.5 μm with the weighted average channel height of 168 nm. The initiation of new dislocation channels in alloy A is substantially less than that in alloy F.

Dislocation loops enhance the formation of dislocation channels and localized deformation in channels. However, while loops provide a sufficient condition for the formation of dislocation channels, dislocation channels may be achieved regardless of the nature of the obstacles as long as the obstacles can be annihilated or weakened by glide dislocations. Cleared channels were also reported in pre-hardened metals by quenching, cold straining, or precipitation [35,36]. The defects under these conditions can be either annihilated or weakened. For instance, vacancy clusters, dislocation loops or stacking fault tetrahedral due to quenching can be annihilated by glide dislocations. Precipitates are usually coherent and can be cut by glide dislocations resulting in a smaller cross-section, which facilitates the glide of subsequent dislocations. It is worth noting that incoherent precipitates which cannot be cut by glide dislocations would not promote dislocation channeling. On the contrary, they promote dislocation cross-slip and homogeneous deformation. This may be the case for voids. Dislocations can cut voids but they leave the voids unchanged, which does not ease the pathway for subsequent dislocations. Void-induced cross-slip [37] may decrease the slip planarity. This may explain why the weighted average channel height decreases with void size and density in Fig. 8c and d.

Stacking fault energy was the parameter used to select the alloys in this study because it was expected to affect the degree of localized deformation. The contribution of SFE to localized deformation is shown in Fig. 11a. As a general trend, localized deformation decreases with increasing SFE. However, alloy B with a low SFE has a very low degree of localized deformation. Fig. 11b and c shows the effect of SFE on dislocation loop size and density. Although the data are scattered, the trend can be seen that the

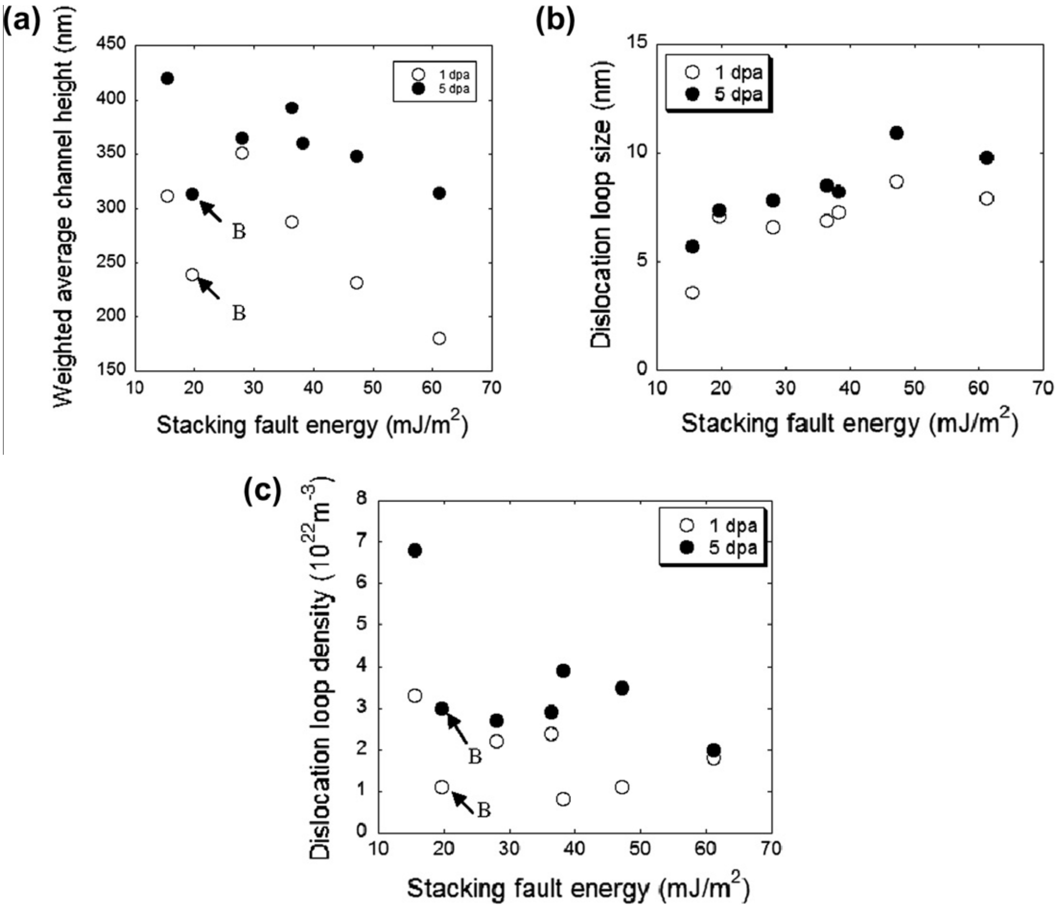

Fig. 11. SFE effect on weighted average channel height (a), dislocation loop size (b) and dislocation loop density (c) in alloys A–G irradiated to 1 and 5 dpa at 360 °C. The weighted average channel height was from alloys strained to 3% at 288 °C in argon.

dislocation loop size increases with SFE while the loop density decreases with SFE. Interestingly, alloy B again does not comply with the trend. Especially for loop density, the value is very low for alloy B. The exception is the same as observed in Fig. 11a. The above observations suggest that SFE probably affects localized deformation by changing irradiated dislocation loop structure and population.

If localized deformation is indeed the primary cause of IASCC, a high density of removable obstacles such as defect clusters, dislocation loops and certain coherent precipitates will be the critical features. Voids, though they can cause problems such as swelling and embitterment of the materials, would not be a concern for IASCC since they do not promote localized deformation. By knowing the contributors to localized deformation, mitigation strategies such as annealing to decrease the density of obstacles that can be annihilated or weakened by moving dislocations may be proposed. Post-annealing experiments already showed that both IGSCC and total dislocation line length decrease with normalized annealing time [1]. Oxide dispersion strengthened (ODS) alloys may be inherently resistant to localized deformation due to the incoherent oxide particles. However, strong evidence of the link between localized deformation and IASCC is still needed.

4. Conclusion

Irradiated microstructure was characterized in seven alloys irradiated to 1 and 5 dpa at 288 °C. Both dislocation loops and voids vary with alloy and irradiation dose. The loop density is significantly higher in the commercial grade alloy A for both doses. Low density of voids was observed in alloys B, D and E at 1 dpa. Voids were observed in all alloys but alloy A at 5 dpa. The largest void size and highest density of voids were observed in alloy B at both doses.

Localized deformation was characterized in proton-irradiated austenitic alloys A–G irradiated to 1 and 5 dpa and strained to 1% and 3% at 288 °C in argon. The weighted average channel height is much smaller in alloys B, F and G. Alloy A irradiated to 5 dpa and strained to 3% has the greatest weighted average channel height. Both irradiation dose and strain promote localized deformation.

Localized deformation was found to be dependent on the irradiated microstructure and to correlate with hardening originating from dislocation loops. Dislocation loops enhance the formation of dislocation channels and the localization of deformation into existing channels. In contrast, voids mitigate the degree of localized deformation.

Correlation between stacking fault energy and localized deformation was observed. The degree of localized deformation decreases with SFE with the exception of alloy B. Alloy B is a low SFE alloy but with a low degree of localized deformation. SFE probably affects localized deformation by changing irradiated dislocation loop structure and population.

Localized deformation may be mitigated by decreasing the density of obstacles that can be annihilated or weakened by moving dislocations or adding incoherent particles that promote dislocation cross-slip.

Acknowledgements

The authors gratefully acknowledge Dr. Ovidiu Toader and Fabian Naab for their assistance in conducting proton irradiations. The authors also acknowledge the facilities provided by the Michigan Ion Beam Laboratory and the Electron Microbeam Analysis Laboratory at University of Michigan. Support for this research was provided by EPRI under contract EP-P20763/C10134 and the Department of Energy (DOE) under contract DE-FG07-05ID14703.

References

[1] J.T. Busby, G.S. Was, E.A. Kenik, J. Nucl. Mater. 302 (2002) 20.
[2] M.C. Hash, J.T. Busby, G.S. Was, in: M.R. Grossbeck, T.R. Allen, R.G. Lott, et al. (Ed.), Proceedings of the 21st International Symposium on Effects of Radiation on Material, ASTM STP 1447. American Society for Testing of Materials, West Conshohocken, PA, 2004, p. 92–104.
[3] T. Onchi, K. Dohi, N. Soneda, J.R. Cowan, R.J. Scowen, M.L. Castano, J. Nucl. Mater. 320 (2003) 194.
[4] T. Onchi, K. Dohi a, N. Soneda, Marta Navas, M.L. Castano, J. Nucl. Mater. 340 (2005) 219.
[5] G.S. Was, J.T. Busby, Philos. Mag. 85 (2005) 443.
[6] Z. Jiao, J.T. Busby, R. Obata, G.S. Was, in: Proceedings of 12th International Conference on Degradation of Materials in Nuclear Power Systems – Water Reactors, The Minerals, Metals and Materials Society, Warrendale, PA, 2005, p. 379.
[7] Z. Jiao, J.T. Busby, G.S. Was, J. Nucl. Mater. 361 (2007) 218.
[8] Z. Jiao, G.S. Was, J. Nucl. Mater. 382 (2008) 203.
[9] J.V. Sharp, in: Proceedings of 4th European Regional Conference on Electron Microscopy, Rome, 1968, p. 417.
[10] J.V. Sharp, Radiat. Eff. 14 (1972) 71–75.
[11] T.S. Byun, N. Hashimoto, J. Nucl. Mater. 354 (2006) 123.
[12] I.M. Robertson, A. Beaudoin, K. Al-Fadhalah, Li. Chun-Ming, J. Robach, B.D. Wirth, A. Arsenlis, D. Ahnc, P. Sofronis, Mater Sci. Eng. A 400–401 (2005) 245–250.
[13] Lucie Saintoyant, Hyon-Jee Lee, Brian D. Wirth, J. Nucl. Mater. 361 (2007) 206.
[14] J.S. Robach, I.M. Robertson, H.-J. Lee, B.D. Wirth, Acta Mater. 54 (2006) 1679–1690.
[15] F.B. Pickering, in: Proceedings of the Conference on Stainless Steels 84, Gothenberg, Sweden, 1984, The Institute of Metals, London, 1985, p. 2.
[16] D. Hull, D.J. Bacon, Introduction to Dislocations, International Series on Materials Science and Technology, vol. 37, Pergamon Press, 1984.
[17] J.F. Ziegler, J.P. Biersack, SRIM2003 Program, IBM Corp., Yorktown, NY.
[18] G. Gupta, Z. Jiao, A.N. Ham, J.T. Busby, G.S. Was, J. Nucl. Mater. 351 (2006) 162.
[19] D.J. Edwards, E.P. Simonen, S.M. Bruemmer, J. Nucl. Mater. 317 (2003) 13.
[20] R.F. Egerton, Electron Energy Loss Spectroscopy in the Electron Microscope, second ed., Plenum Press, New York, 1996.
[21] G.S. Was, J.T. Busby, Z. Jiao, Final Report, EPRI Project EP-P3038/C1434, September 2005.
[22] S.M. Bruemmer et al., Final Report, EPRI Project WO4068-20, November 2000.
[23] L. Vitos, J.-O. Nilsson, B. Johansson, Acta Mater. 54 (2006) 3821–3826.
[24] F.A. Garner, W.G. Wolfer, J. Nucl. Mater. 102 (1981) 143.
[25] J.F. Bates, J.J. Holmes, M.M. Paxton, J.L Straaslund, US Patent. 3856,517, 1974.
[26] W.G. Johnston, T. Lauritzen, J.H. Rosolowski, A.M. Turkalo, in: N.L. Peterson, S.D. Harkness (Eds.), Radiation Damage in Metals, American Society of Metals, 1975, p. 221.
[27] T.R. Allen, J.I. Cole, J. Gan, G.S. Was, R. Dropek, E.A. Kenik, J. Nucl. Mater. 342 (2005) 90–100.
[28] J.T. Busby, M. Hash, G.S. Was, J. Nucl. Mater. 336 (2005) 267.
[29] A. Seeger, in: Proceedings of 2nd UN International Conference On Peaceful Uses of Atomic Energy, Geneva, September 1958, vol. 6, p. 250.
[30] G.S. Was, Fundamentals of Radiation Materials Science: Metals and Alloys, Springer, Berlin, 2007.
[31] G.I. Taylor, J. Inst. Metal. 62 (1938) 307.
[32] K. Farrell, T.S. Byun, N. Hashimoto, J. Nucl. Mater. 335 (2004) 471.
[33] D.J. Edwards, B.N. Singh, J.B. Bilde-Sørensen, J. Nucl. Mater. 342 (2005) 164.
[34] H. Neuhäuser, R. Rodloff, Acta Metal. 22 (1974) 375.
[35] A.J.E. Foreman, J.V. Sharp, Philos. Mag. 19 (1969) 931.
[36] A. Luft, Prog. Mater. Sci. 35 (1991) 97.
[37] Tetsuya Kaneko, Yousuke Abe, Hideki Matsui, Phys. Rev. B 77 (2008) 064108.